Journal of Manufacturing Processes 118 (2024) 228–241

Contents lists available at ScienceDirect

Journal of Manufacturing Processes

journal homepage: www.elsevier.com/locate/manpro

Integration of space-holder technique and spark plasma sintering: An innovative approach for crafting radially graded porosity implants

Ricardo Chávez-Vásconez [a,b], Daniel Auger-Solís [a], Eva M. Pérez-Soriano [b], Cristina Arévalo [b,*], Isabel Montealegre [b], Javiera Valencia-Valderrama [a], Mauricio Reyes-Valenzuela [a], Carolina Parra [a], Rodrigo Segura-del Río [c], Yadir Torres [b], Sheila Lascano [a,*]

[a] Departamento de Ingeniería Mecánica, Universidad Técnica Federico Santa María, Avenida Vicuña Mackenna 3939, Santiago 8940572, Chile
[b] Departamento de Ingeniería y Ciencia de los Materiales y del Transporte, Escuela Politécnica Superior, Universidad de Sevilla, Calle Virgen de África 7, Sevilla 41011, Spain
[c] Facultad de Ciencias, Universidad de Valparaíso, Avenida Gran Bretaña, Valparaíso 7590943, Chile

ARTICLE INFO

Keywords:
Functionally graded porous materials
Titanium alloys
Powder metallurgy
Spark plasma sintering
Field assisted sintering technologies
Radial graded porosity

ABSTRACT

Bone resorption and possible fracture of host tissue are some consequences resulting from the mismatch between the Young's Modulus of the constituent materials of implants and bone that compromises the reliability of implants for replacing damaged bone tissue. The use of functional graded porous materials presents an interesting approach that could help decrease the Young's modulus while simultaneously mimicking highly hierarchical porosity of the bone structure. However, these structures are more difficult to fabricate than those with homogenous porosity. The design and distribution of this porosity in the implant must ensure the biomechanical and biofunctional balance of the bone tissue it is intended to replace. In this study, Ti radially graded structures were successfully fabricated using Spark Plasma Sintering combined with Space Holder Technique. The effects of temperature on porosity and mechanical properties were thoroughly examined. The results indicated that this processing route allows to achieve good control of porosity, close to the amount of added spacer. Yield stress of 181 MPa and an elastic modulus of 56 GPa were obtained for samples sintered at 800 °C for 5 min under a pressure of 6.3 MPa. These mechanical properties make the structure a viable candidate for replacing human long bones.

1. Introduction

Bone degradation has been identified as one of the primary causes of reduced mobility and well-being in the elderly [1]. In fact, adults over the age of 35 are the group most affected by reduction in bone density [2–4], with a reported 40 % reduction in strength that could be further increased by the combined action of cyclic loading degradation and surface wear of the joints [5] Additionally, there are other contributing factors, such as (i) an increase in life expectancy in developed countries and (ii) a growing demand for different types of implants to replace failing parts, particularly in young patients. The first factor is related to the fact that the world's population is ageing [6,7]. In recent years, the number of people aged 60 years or over, the "older", and those aged 80 years or over, the "oldest-old", has increased substantially in most countries and regions, and this trend is expected to accelerate in the coming decades [8]. The second aggravating factor is the increasing demand for different types of implants used to replace the knee, hip, elbows, and shoulder, due to reasons such as fractures [9], replacement of broken parts, accidents [10] or aesthetic procedures [6,11–14]. Approximately, 10–15 % of implants have been reported to fail before 10 years of permanent use, leading to 20 % of implant surgeries being performed to correct failed procedures [15]. This aspect is particularly relevant in young patients who require longer-lasting prostheses and/or implants to return to a normal life, implying higher load levels [15].

Metallic biomaterials are commonly used materials for bone tissue replacement and load-bearing applications. Among them, Ti-based

* Corresponding authors.
E-mail addresses: ricardo.chavezv@usm.cl, ricchavas@alum.us.es (R. Chávez-Vásconez), daniel.auger@sansano.usm.cl (D. Auger-Solís), evamps@us.es (E.M. Pérez-Soriano), carevalo@us.es (C. Arévalo), imontealegre@us.es (I. Montealegre), javiera.valencia@sansano.usm.cl (J. Valencia-Valderrama), mauricio.reyes@usm.cl (M. Reyes-Valenzuela), carolina.parra@usm.cl (C. Parra), rodrigo.segura@uv.cl (R. Segura-del Río), ytorres@us.es (Y. Torres), sheila.lascano@usm.cl (S. Lascano).

https://doi.org/10.1016/j.jmapro.2024.03.056
Received 10 January 2024; Received in revised form 1 March 2024; Accepted 18 March 2024
Available online 22 March 2024

materials are widely demanded due to their most suitable characteristics for biomedical applications, such as their excellent mechanical properties (yield strength 170–483 MPa and tensile strength 240–550 MPa), low density, corrosion resistance, and adequate response both in vitro and in vivo [16]. However, titanium and its alloys present a significant drawback, which is the difference between the stiffness of titanium (~100–110 GPa) and bone tissue (~2–30 GPa), leading to the phenomenon of stress-shielding [17]. This phenomenon compromises the reliability of implants by promoting bone resorption and possible fracture of host tissue [18], risking appropriate implant performance [19]. An effective approach to minimise this phenomenon is to reduce the Young's modulus of the biomaterial by modifying the micro and mesostructure [20].

One of the strategies employed to decrease the Young's modulus is to introduce porosity into the structure. In this sense, metallic porous biomaterials have demonstrated a lower elastic modulus than their fully dense counterparts [21,22], which can be similar to that of the host bone, reducing the phenomenon of stress-shielding, and promoting cell proliferation and differentiation [23]. Powder metallurgy is a manufacturing process that can be utilised to obtain porous structures when combined with the space-holder technique, as it offers the possibility of produce customised porous titanium samples for biomedical applications in a cost-effective way [20]. The combination of this method with the space holder technique emerges as an effective way to provide high levels of porosity (35–80 %) with a homogeneous distribution in the samples, with a pore size suitable for cell growth (50–400 μm) [24]. Various materials are regularly used as temporary space holder particles, including ammonium bicarbonate [25–27], carbamide [24], K_2CO_3 [28], polymethyl methacrylate (PMMA) [29,30], and polyvinyl alcohol (PVA) [31], which are subsequently removed by evaporation at low temperatures. Sodium chloride is another space holder that is removed by dissolution in water [17,26,32–35] and presents several advantages, such as low cost, easy dissolution, and negligible residual toxicity [36]. However, while this combination of techniques increases porosity, leading to a reduction in Young's modulus, it also decreases mechanical strength, falling below the required level for bone replacement [37,38]. Therefore, the aim is to achieve a balance between the benefits of high and low porosity by creating functionally graded porous materials (FGPMs), which are porous structures with porosity gradients distributed over its volume [39,40]. In biomedical field, the FGPMs is considered an innovative strategy for enhancing the performance of implants with advantages over monolithic materials, because the gradual transitions of porosity introduce functional changes in its properties and reduces the stress shielding [40,41]. In this sense, radially graded porous distribution with porosity levels of 60 %, 40 %, and 20 % from the centre outwards to obtain materials with suitable mechanical strength and low elastic modulus while mimicking the structure of bone [40]. Wang *et al.* [42] have studied the application of porosity graded structure in the design of femoral stem in order to relieve the bone resorption and promoting osseointegration by finite element analysis. The best performance for radial gradients was found to be the one with a porosity increased inwardly, i.e. the densest layer is the external one. In this sense, the fabrication of materials which exhibits the mentioned porosity gradient is attractive due to its potential for its use in applications where the stress distribution has to be controlled to avoid stress concentration as in femoral stem, or intervertebral disks [43,44].

Generally, FGPM biomaterials are more challenging to fabricate compared to uniform or homogenous biomaterials [43,45]. A functionally graded pore distribution can be achieved through a few methods, such as, additive manufacturing [46–51], powder metallurgy [36], creep expansion of argon-filled pores and electric current activated/assisted sintering [37,52–56]. Various hot consolidation techniques have been used to manufacture this type of components, including hot press sintering [57], hot isostatic pressing [57], and Field Assisted Sintering Technique/Spark Plasma Sintering (FAST/SPS) [21,58–62]. In particular, FAST/SPS offers the advantage of high heating and cooling rates, resulting in a short processing time that significantly enhances mechanical properties and inhibits grain growth at relatively low temperatures [62–66].

In previous work, Torres et al. [67] obtained titanium structures with radial porosity gradient using the space-holder technique and sintering in a tube furnace. A device designed to compact, in a sequential manner, structures with a radial distribution was designed and implemented [68,69]. The device can produce radial gradient porous structures from metallic and ceramic powders, but could also be used to produce gradients of functional composition [70,71]. For the design of these structures, the densest layer was considered in the centre, and the most porous layer in the outer layer, resulting in a stiffness of 8.3 GPa and a Yield stress of 278 MPa. It can be observed that the stiffness of the sample is low in relation to what is required for the replacement of cortical bone, which may be due to the fact that when manufacturing the outer layer (which corresponds to the layer with the highest volumetric fraction) is manufactured with higher porosity, suitable to withstand lower loads, to promote bone ingrowth or for the replacement of trabecular bone. Conventional sintering of titanium, however, requires long sintering times and the use of inert atmospheres or high vacuum to avoid oxidation problems, which can impair the mechanical properties of the part.

Yilmaz et al. [72], fabricated a FGPM consisting of a core of porous Ti and a dense Ti-HA outer layer using conventional sintering. The sintering was made at 1200 °C for 2 h and reached a porosity level of 58 % for the core, and a porosity level of 29 % for the outer layer, which are aimed to mimic the trabecular and cortical bone, respectively. The mechanical results obtained by means of nano-indentation showed that the FGPM exhibited elastic moduli of 19 and 43 GPa for the inner and outer layers, respectively. Those results suggested the adequate use of the produced structure for bone replacement, and the cell viability study showed an improve of the biological properties. Nonetheless, the production of the mentioned FGPM is a long process due to the heating and cooling rates that can be achieved using conventional sintering.

For their part, Zhang et al. [73] synthesised homogeneous samples with 38 % porosity sintered by SPS, non-conventional sintering process, using NH_4HCO_3 as a spacer, obtaining a stiffness of 11.2 GPa and a compressive strength of 287 MPa. In this case, a special matrix was necessary to avoid applying pressure on the sample in order to control porosity and densification. Baghtifouni et al. [74], for its part, achieved a titanium sample with a longitudinal porosity gradient with layers of 30/60/70/60/30 vol%, NaCl through SPS sintering, which had adequate stiffness for bone tissue replacement. With the latter, it can be demonstrated that it is possible to achieve a porosity gradient through SPS, but to the best of our knowledge to date, no studies have been carried out with a functional radial porosity gradient through the SPS sintering and space holder technique.

In this study, a new route of fabrication for titanium structures which exhibit radial porosity gradient has been developed. In the developed route, the SPS was carried out using conventional tooling and sintering without the space-holder particles, allowing the whole fabrication cycle to be more efficient than the existing routes reported up to date, in terms of versatility, repeatability, and cost-effective when compared to the processes reported up to date in order to achieve controlled porosity gradients. The objective of this research is to develop, process, and characterise Ti samples with a decreasing porosity gradient from the centre to the surface, obtained by the space holder technique using NaCl as a temporary spacer particle, and consolidated by FAST/SPS. The main goal is to enhance the mechanical strength of the sample by achieving an optimal porosity distribution. This will allow the layer with the highest volumetric fraction to withstand higher loads, while simultaneously obtaining a stiffness similar to that of bone by incorporating greater porosity in the centre and mimicking its structure. The proposed structure is intended to have similar properties of long bones which exhibit a radial gradient with a porous core (trabecular bone) and a dense outer

layer (cortical bone).

2. Materials and methods

2.1. Preparation and characterisation of the starting materials

Titanium powder grade 4 (Alfa Aesar, USA) was selected as the matrix material, while sodium chloride (Loba Chemie, India) was used as spacer particles. To control the pore size, sodium chloride particles with a size in the range of 100–400 μm were chosen [75]. The sieving of the NaCl particles was carried out in a Gilson® SS3 device (Gilson Incorporated, USA), with 40 and 140 mesh sieves, according to the ASTM E11 standard [76]. This technique used to restrict the particle size was selected to limit pore size, as for implant applications it has been found that this factor could affect cell growth and proliferation [77].

Prior to the consolidation stage, a morphological analysis of the starting powders and NaCl particles was conducted using Scanning Electron Microscopy (SEM) with a Quattro S SEM microscope (Termo Fischer Scientific, USA), following the ASTM standard F1877 [78]. Titanium particle size analysis was performed by means of laser beam diffraction with an Analysette 22 unit (Frisch GmbH, Germany). Once the starting materials were characterised, the specimens for further study were manufactured.

2.2. Preparation of green and sintered FAST/SPS samples

Before the consolidation of the samples, various mixtures that construct the radial porosity gradient were prepared. Table 1 displays the various proportions of titanium and NaCl that were employed. To ensure complete homogenisation, each combination was blended for 40 min on a TURBULA® T2F mixer (WAB, Switzerland). The quantity of powders prepared was determined based on the final dimensions of the test cylinders, which are 16 mm in height and 20 mm in diameter (height/diameter = 0.8), in accordance with ISO 13314 [79] and ASTM E9 [80].

Then each mixture was uniaxially compacted with a Zwick/Roell Z100 universal testing machine (Zwick/Roell, Germany). In order to create the radial gradient, a sequential compaction device was employed. The compaction process involved the following successive steps shown in Fig. 1.

1. Core compaction: The bushings were assembled in the compaction matrix, leaving a free space of 8 mm in diameter. This space was then filled with the mixture corresponding to the core (Blend 1), which was compacted at 500 MPa with an advance speed of 3 mm/min, and a holding time of 2 min. Afterward, the core was extracted and prepared for the next stage.
2. Compaction of the intermediate layer: The compaction matrix was assembled with the external sleeve, leaving a free space of 14 mm in diameter. The compacted core was placed on the lower base using petroleum jelly to prevent movement, and the punch was centred to clear the space that will be occupied by the intermediate layer. The space was filled with the mixture corresponding to the intermediate layer (Blend 2) and compacted under 400 MPa with an advance speed of 3 mm/min and a holding time of 2 min. Subsequently, the green compact was extracted, ready to be compacted in the final stage.
3. Compaction of the external layer: The green compact was positioned on the lower base using one drop of petroleum jelly to prevent movement, and the punch was centred to clear the 20 mm diameter space that the outer layer will fill. The die cavity was then filled with the Blend 3, corresponding to the external layer, and compacted under 300 MPa with an advance speed of 3 mm/min and a holding time of 2 min. At this point, the final green compact was extracted and ready with the radial gradient.

Table 1
Proportions of Ti and NaCl used to obtain the porous graded samples.

	Layer	vol% Ti	vol% NaCl
Blend 1	Internal	40	60
Blend 2	Intermediate	60	40
Blend 3	External	80	20

After green consolidation, the spacer particles were removed, prior to sintering of the samples, by dissolution in the distilled water at 50 °C (without agitation). In order to prevent NaCl saturation in the distilled water and facilitate spacer removal, the water was replaced every 2 h by suction to avoid any manipulation of the samples. During this removal cycle, drying steps were performed every 4 h in an oven at 110 °C for 40 min. The mass loss was measured after each cycle to ensure the elimination of NaCl. The process was finished when the mass loss stabilised.

Subsequently, sintering was conducted using a FAST/SPS KCE®-FCT HP D-10 equipment (FCT Systeme GmbH, Germany), with a 20 mm diameter graphite matrix and punches. The green samples were sintered under a uniaxial pressure of 6.3 MPa in a high purity (99.95 %) argon atmosphere. The sintering process consisted of two stages: firstly, the samples were heated up to 600 °C at a rate of 150 K/min, followed by an increase in the sintering temperature (700 and 800 °C) at a rate of 50 K/min. The dwell time was 5 min, and then the samples were cooled at an approximate rate of 350 K/min. The sintering process was conducted with DC current without pulses. The sintering curves are depicted in Fig. 2. After sintering, the samples were characterised to analyse their physical, microstructural, and mechanical properties.

2.3. Physical and microstructural characterisation of the sintered samples

Given that the manufacturing process employed in this study involves applying pressure to the sample during sintering, it is imperative not to neglect the dimensional changes (i.e., shrinkage). To assess shrinkage, both the diameter and height dimensions of the cylindrical samples were measured before (in their green state) and after sintering stage, using a digital Vernier calliper. By comparing measurements of these dimensions, the volumes of both the green and sintered samples were calculated, allowing for the quantification of the shrinkage percentage.

The Archimedes' method of distilled water impregnation was used to estimate the density of the sintered samples due to its experimental simplicity and reasonable reliability (ASTM B962) [81]. This method utilises the mass of the specimen under various conditions: in air, impregnated, and immersed in distilled water. The total porosity, P_T, and interconnected porosity, P_i, were calculated on the basis of the density values obtained. With these values, it can be determined whether the structure exhibits a closed-cell or an open-cell configuration.

For the microstructural analysis, the specimens were then prepared following conventional metallographic procedures according to ASTM E3 [82]. The final step involved mechanical-chemical polishing using colloidal silica and hydrogen peroxide. The size, morphology, and porosity distribution were analysed through image analysis (IA) of micrographs obtained by Optical Microscopy (OM) using a Nikon Eclipse MA100N microscope (Nikon Corporation, Japan) and by Scanning Electron Microscopy (SEM) on a FE-SEM Thermoscientific Quattro S (Thermo Fisher Scientific, USA). Image analysis was conducted using Image-Pro Plus® software (Media Cybernetics, USA). The following porosity parameters were characterised: (i) total porosity obtained by image analysis ($P(IA)$); (ii) equivalent pore diameter (D_{eq}), defined as the average porosity diameter measured from the centroid of the pores; (iii) pore shape factor (F_f); and (iv) mean size of the neck between pores (micropores resulting from the powder metallurgy process: λ_{pm}; macropores produced by the spacer particles: λ_{sh}). The results were

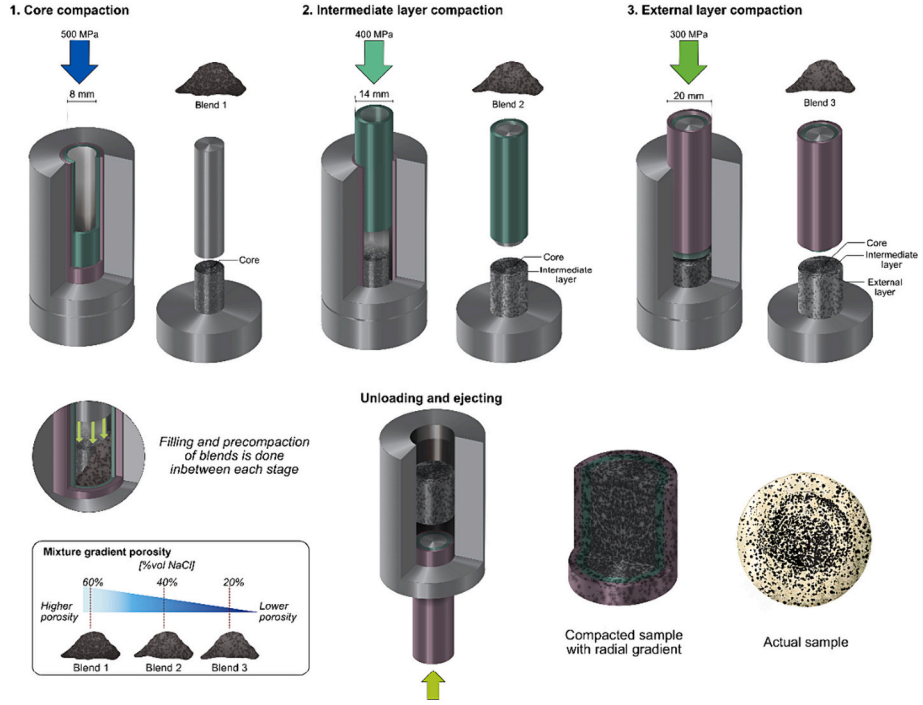

Fig. 1. Sequence of steps applied for the fabrication of green samples to obtain a radially distributed porosity gradient. Each layer contains a different percentage of the spacer.

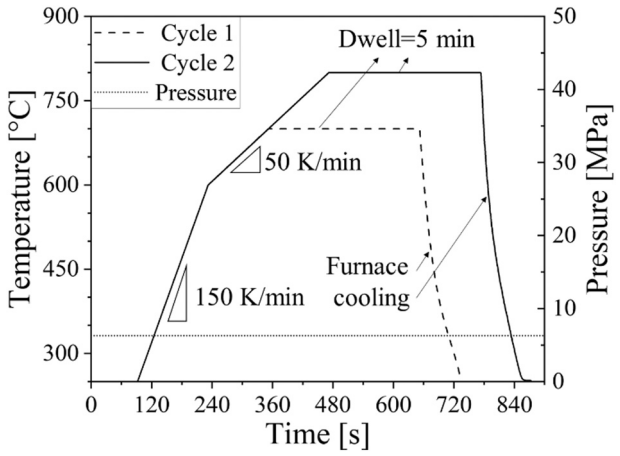

Fig. 2. Sintering curves employed to produce the studied samples.

expressed as mean ± standard error. A mean difference test was performed to determine the influence of the sintering temperature on the equivalent diameter of the pores and the pore shape factor, with a significance level of $p_{value} < 5$ %. The pore morphology and interfaces in the functionally graded porous materials (FGPM) samples were analysed using SEM Thermoscientific Quattro S (Thermo Fisher Scientific, USA).

Surface roughness was also measured using a Mitutoyo SJ-310 roughness gauge (Mitutoyo, Japan). The parameters measured according to ISO 4287 [83] were: (i) arithmetical mean roughness (R_a), (ii) root mean square roughness (R_q), (iii) mean height of the profile (R_c), and (iv) maximum height of the profile (R_z).

2.4. Mechanical characterisation of the sintered samples

Microhardness measurements were performed using a LECO LM 300AT microdurometer (LECO, USA) equipped with a Vickers indenter. A load of 98.07 mN was applied for 7 s, and at least 20 measurements per sample were made in areas without pores to avoid the measures could be affected by this stress intensity factor. Furthermore, nanoindentation tests were conducted using an iNano nanoindenter (Nanomechanics INC, USA) equipped with a Berkovich diamond indenter. Prior to indentation, the calibration was done following the Oliver-Pharr method [84] in fused silica. The nanoindentation test was carried out with a load of 50 mN for 1 s and a strain rate of 0.2 s^{-1}.

Furthermore, leveraging the results of the modulus of elasticity by nanoindentation and the porosity determined through image analysis, an estimation of the modulus of elasticity and yield stress of the functionally graded porous structure was performed. Since each layer had a different percentage of porosity, the mechanical properties of each layer were estimated.

The modulus of elasticity was evaluated using the Nielsen eq. [85] as follows:

$$E_p = E_s \cdot \frac{(1-P)^2}{1+\left(\frac{1}{F_f}-1\right)\cdot P} \tag{1}$$

where E_p is the modulus of elasticity of each porous layer, E_s is the modulus of elasticity of the substrate material, P is the percentage of porosity, and F_f is the pore shape factor.

To estimate the yield stress, the correlation proposed by Jha et al. [86] was used:

$$\sigma_{y,p} = 0.74 \cdot \sigma_{y,s} \cdot \left(\frac{\rho_p}{\rho_s}\right)^{2.206} \tag{2}$$

where $\sigma_{y,p}$ is the yield stress of each porous layer, $\sigma_{y,s}$ is the yield stress of the substrate material, ρ_p is the density of the porous layer, and ρ_s is the density of the substrate material.

Using the mechanical properties obtained for each layer, the mechanical properties of the complete structure with radial gradient behaviour were estimated using the mixing rule (ROM) with a correction factor. This was determined on the basis of the findings of Wu et al. [87], assuming that the layers in the gradient structure had similar

thicknesses. Thus, the expression used to estimate the mechanical properties was:

$$X_T = n_x \cdot \sum_{i=1}^{3} (X_i \cdot V_i) \quad (3)$$

where X_T is the estimated mechanical property X of the gradient structure, n_x is the correction factor for the property X, X_i is the value of the mechanical property of the umpteenth layer, and V_i is the volume fraction of the umpteenth layer. In the proposed structure, the volume fractions are 51 %, 33 % and 16 % for the external, intermediate and internal layer, respectively. For gradient structures with layers of similar thickness, the correction factors were 1.36 for the modulus of elasticity and 1.13 for the yield stress.

3. Results

3.1. Characterisation of the starting powders

SEM images of titanium powders and NaCl particles, along with their particle size distributions, are presented in Fig. 3. The titanium particles exhibit an irregular morphology, ranging in size from 5 to 100 μm, with a mean particle size of 50 μm. In contrast, NaCl particles display a polygonal shape and vary in size from 50 to 700 μm, with an average particle size of 250 μm. Understanding these parameters is crucial due to the speed of the sintering process used, in order to determine the holding capacity of the geometry capacity for future applications.

3.2. Physical and microstructural characterisation of the sintered samples

The dimensions of the green and sintered samples, along with the calculated volume, geometric density, and shrinkage, are summarised in Table 2. It can be seen that the diameter tends to increase, while the height decreases. This behaviour can be attributed to the compacting pressure applied to the sample during the sintering stage and the clearance between the green sample and the graphite die used for sintering. Comparing the calculated volumes (assuming a bulk cylinder), shrinkages of 15.79 % and 21.07 % were observed for the samples sintered at 700 °C and 800 °C, respectively.

Micrographs obtained by OM of the samples of Ti grade 4 with radially graded porosity obtained by space holder technique and FAST/SPS are shown in Fig. 4. Each group of figures surrounds the cross-sectional image of the corresponding sample. In general, a radial gradient porous distribution is observed; the porosity increases gradually to the centre of the sample, bioinspired in the gradual porosity of human bones, such as, femoral stem, or intervertebral disks. In both cases, the three gradient zones as well as the interlayers are differentiated, as will be discussed below, the porosity in each zone is in accordance with the spacer content used. In general, the structural integrity of the interfaces is good, where the three layers are clearly visible. The most noticeable interfaces are those between the external layer and the intermediate layer, due to the lower porosity of that. Fig. 4 (a) – (e) depict the zones that constitute the sample sintered at 700 °C: (a) external layer, (b) intermediate layer, (c) internal layer, and their respective interfaces: (d) interface 1- between the external layer and intermediate layer and interface 2- between the intermediate layer and the internal layer. Fig. 4 (f) – (j) show the zones that constitute the sample sintered at 800 °C. As it is observed, the sample sintered at 800 °C exhibits a higher densification and better joining at interfaces, showing a gradual transition when compared to the sample sintered at 700 °C.

In addition, SEM images show the regions of interest on the fabricated samples (Fig. 5). In Fig. 5 (a) and (b) the interface between the Ti powder particles forming the consolidated material can be observed and the Fig. 5 (c) and (d) show the interface between the external layer and the intermediate layer of both samples. Both cases have an accentuated interface due to an orderly particle arrangement brought about by the compaction phase. The Fig. 5 (e) and (f) depict the interface between the intermediate layer and the internal layer of each sample, respectively. This region, with a high probability of pore coalescence, causes the

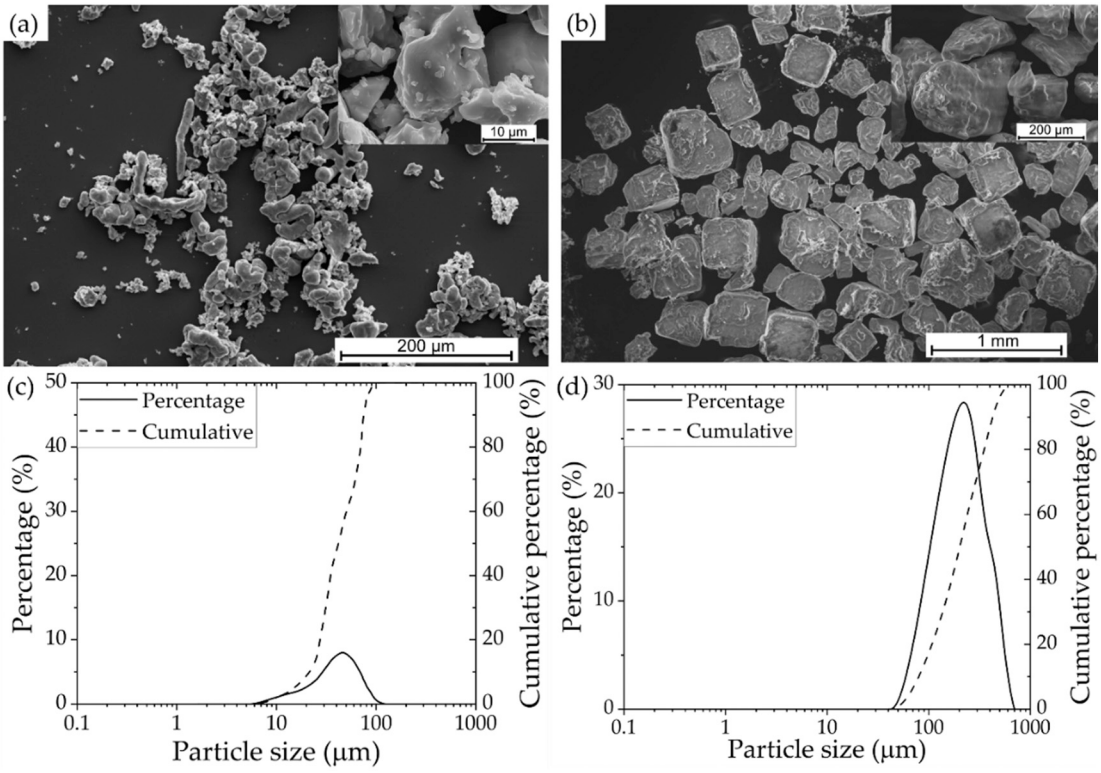

Fig. 3. SEM images of particles: (a) Ti; and (b) NaCl; Particle size distribution of: (c) Ti; and (d) NaCl.

Table 2
Characteristic dimensions of green and sintered samples.

Sintering temperature [°C]	Sample state	Diameter [mm]	Height [mm]	Volume [cm^3]	Density [g/cm^3]	Shrinkage [%]
700	Green	19.98 ± 0.02	12.59 ± 0.04	3.947 ± 0.029	2.34 ± 0.02	15.79 ± 0.30
	Sintered	20.02 ± 0.03	10.56 ± 0.05	3.324 ± 0.036	2.86 ± 0.03	
800	Green	19.97 ± 0.07	12.82 ± 0.09	4.015 ± 0.080	2.33 ± 0.05	21.07 ± 1.01
	Sintered	20.18 ± 0.03	9.91 ± 0.02	3.170 ± 0.022	3.05 ± 0.02	

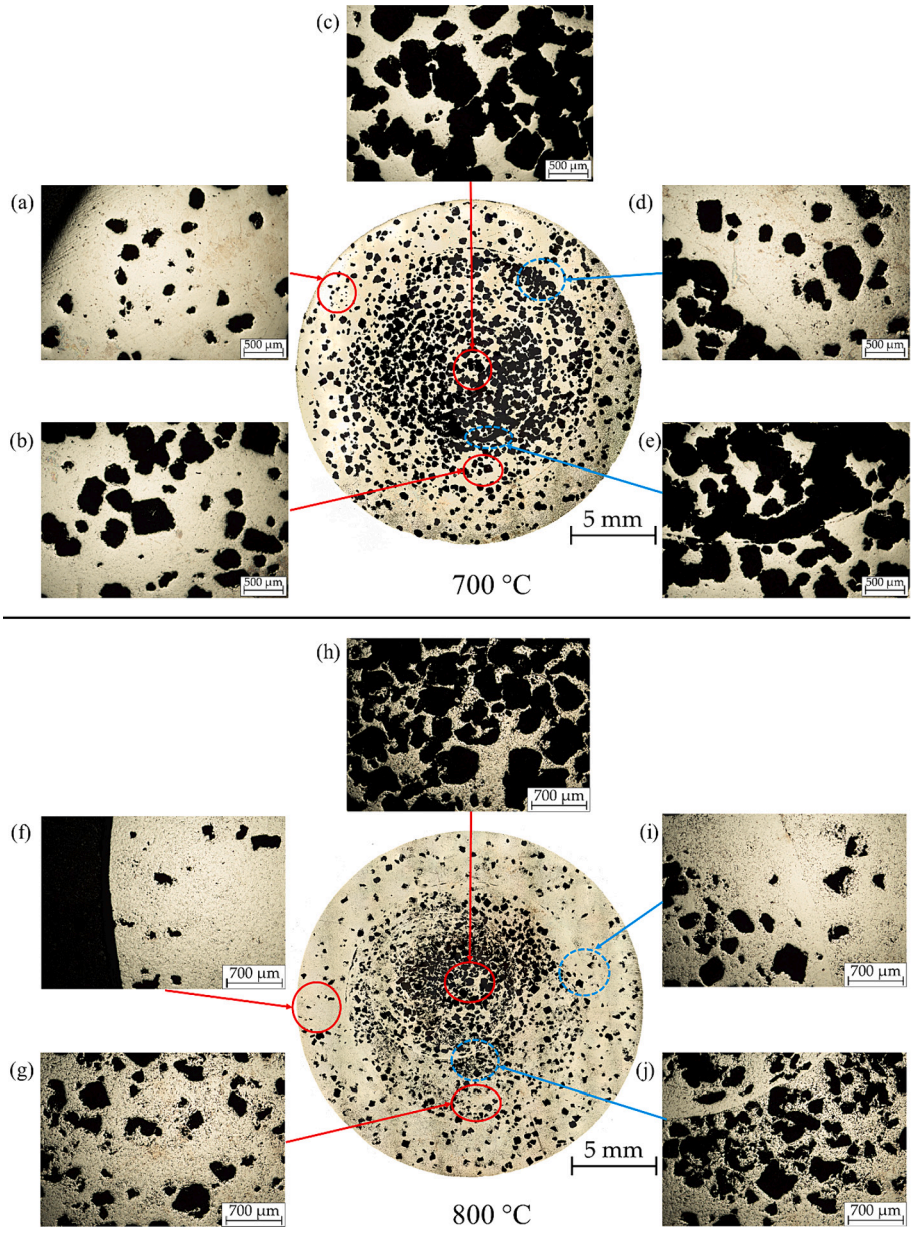

Fig. 4. Micrographs obtained by OM of Ti structures with a porosity gradient produced by SPS. Sample sintered at 700 °C: (a) external layer; (b) intermediate layer; (c) internal layer; (d) interface 1; and (e) interface 2. Sample sintered at 800 °C: (f) external layer; (g) intermediate layer; (h) internal layer; (i) interface 1; and (j) interface 2.

formation of elongated defects in the interface. According to Fig. 5 (c), the junction like-crack in the sample sintered at 700 °C is approximately three times wider than that in the sample sintered at 800 °C, and the gap is even visible in the overview shown in Fig. 4 (f). Nonetheless, from a general standpoint, it is difficult to distinguish the presence of the elongated defects in the sample sintered at 800 °C (Fig. 4 (l)). Finally, Fig. 5 (g) and (h) provide detailed images of the pores that can be found in the structure. It is observed that the pores, despite having a polygonal geometry, due to the spacer geometry, present rounded corners.

Fig. 6 shows frequency distribution histograms of the pore sizes found in the fabricated samples, showing the contribution of each layer. The Table 3 compiles the information obtained from the image analysis,

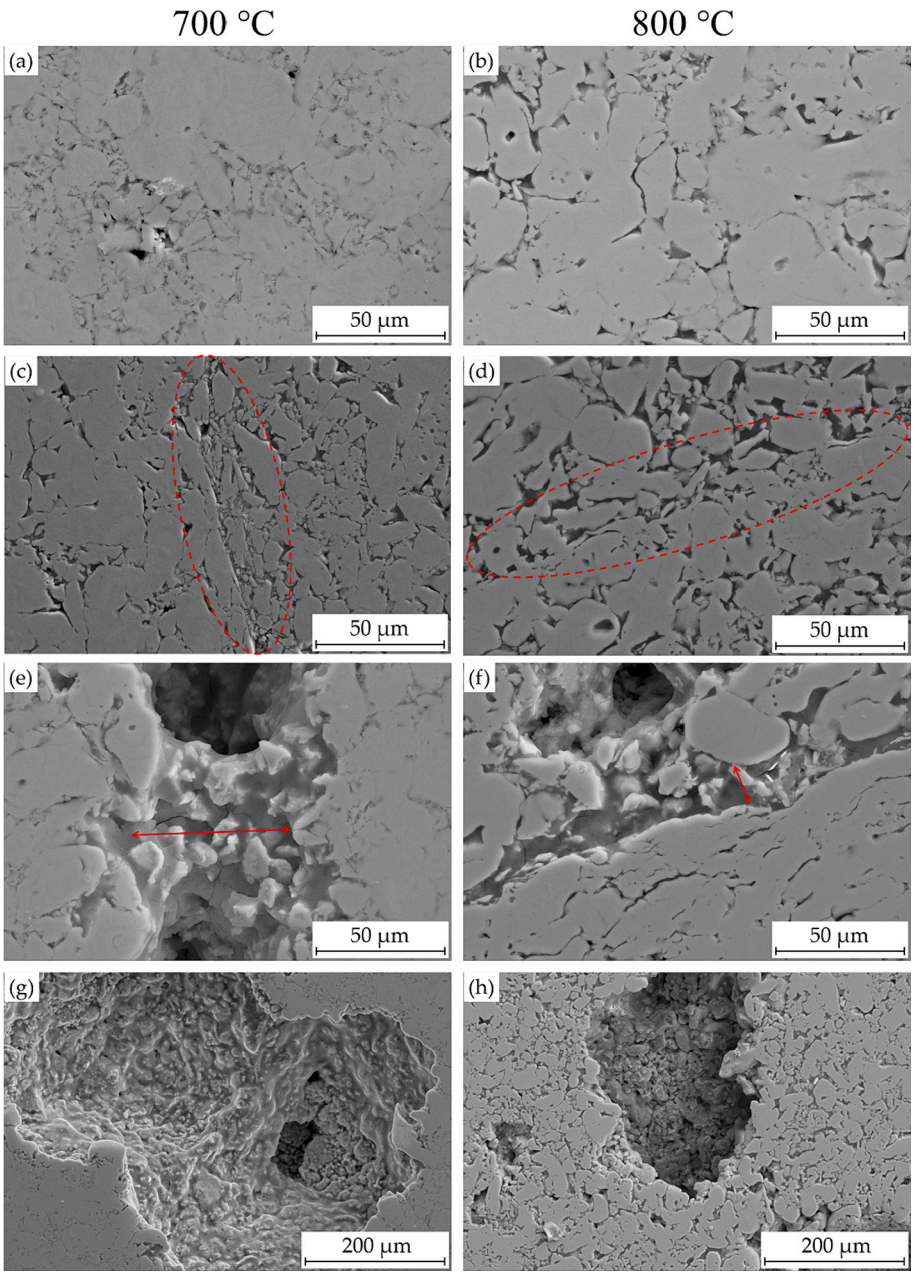

Fig. 5. SEM images of regions of interest of Ti structures with radially graded porous structure obtained through FAST/SPS. Sample sintered at 700 °C: (a) Surface; (c) Interface 1; (e) Interface 2; and (g) Pore. Sample sintered at 800 °C: (b) Surface; (d) Interface 1; (f) Interface 2; and (h) Pore.

separated by each layer that forms the structures with gradient porosity, and the results of the Archimedes' test and the porosity obtained through image analysis for the entire samples. All the information presented in these tables is given in terms of the mean ± standard error.

From the Archimedes' test, it was determined that the total porosity and interconnected porosity for the sample sintered at 700 °C are 40.6 % and 41.3 %, respectively. For the sample sintered at 800 °C, the values of total porosity and interconnected porosity are 33.8 % and 34.6 %, respectively. In both cases, it is observed that the porosity is predominantly interconnected.

In terms of porosity, the differences between the values obtained in the samples sintered at 700 °C with respect to those obtained at 800 °C are 9.2 %, 3.4 %, and 8.2 % for the external, intermediate, and internal layers, respectively. The porosity of the sample sintered at 700 °C is higher than those of the specimen obtained at 800 °C. However, considering the initial design of the porosity of the sample, based on the percentage of added spacer particles, selecting 800 °C as the sintering temperature results in a porosity very close to the design values (18.2 % ± 1.9; 42.7 % ± 1.6 and 57.4 % ± 4.1 vs 20 %, 40 and 60 vol% NaCl).

Furthermore, the equivalent pore diameter (D_{eq}) for both samples ranges from 50 µm to 900 µm, as shown in Fig. 6. The same Fig. 6 highlights that the layer that contributes most of the pores is the external layer of each sample.

The porosity distribution shows that, for both sintering temperatures, 95 % of the porosity consists of pores up to 500 µm and, in Fig. 4, it is observed that the pore size in the internal layers is larger than the pore size in the external layers.

The calculated pore shape factor was 0.82 and 0.62 on average for the samples sintered at 700 °C and 800 °C, respectively. Regarding the pore shape factor of each layer, it can be observed that the internal layers have the lowest values, being 0.65 and 0.45 for the samples sintered at 700 °C and 800 °C, respectively.

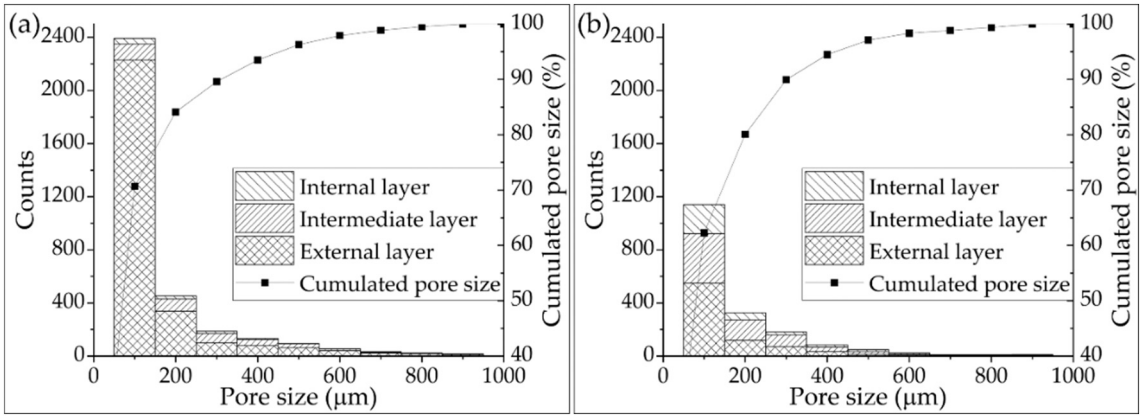

Fig. 6. Pore size distribution of samples sintered at: (a) 700 °C; (b) 800 °C.

Table 3
Porosity parameters of samples and total porosity obtained by means of the image analysis (IA) and Archimedes' test.

Sintering temperature	Layer	Image analysis					Archimedes' test	
T_{sint}		D_{eq}	F_f	λ_{sh}	$P(IA)$	$P(IA)^*$	P_{int}	P_T
[°C]		[μm]		[μm]	[%]	[%]	[%]	[%]
700	External	187 ± 24	0.85 ± 0.22	710 ± 245	27.5 ± 4.6	39.8 ± 2.6	40.6 ± 0.4	41.3 ± 0.3
	Intermediate	313 ± 17	0.64 ± 0.20	425 ± 116	46.1 ± 1.8			
	Internal	381 ± 55	0.65 ± 0.22	276 ± 121	65.7 ± 3.7			
800	External	141 ± 24	0.73 ± 0.29	1257 ± 459	18.2 ± 1.9	32.6 ± 1.4	33.8 ± 0.4	34.6 ± 0.3
	Intermediate	245 ± 23	0.52 ± 0.22	568 ± 129	42.7 ± 1.6			
	Internal	293 ± 71	0.45 ± 0.20	340 ± 182	57.5 ± 4.1			

* Calculated using the ROM of Eq. (3).

The microporosity values were 15 μm and 22 μm for the samples sintered at 700 °C and 800 °C, respectively. On the other hand, macroporosity values are in the range of 340–950 μm and 270–650 μm for the samples sintered at 700 °C and 800 °C, respectively. The difference between these ranges is much greater than the difference found between the distances of microporosity.

Table 4 summarises the parameters obtained in the roughness test performed on the samples with gradient porosity. The results were expressed in terms of mean ± standard deviation, where the R_a values are 19.01 μm and 10.81 μm for the samples sintered at 700 °C and 800 °C, respectively.

3.3. Mechanical characterisation of sintered samples

In addition to the study of surface characteristics and porosity, which can affect cell adhesion and proliferation, assessing the mechanical properties is also important to ensure the proper mechanical performance of the porous structure. The microhardness values obtained by means of conventional microindentation are 205.02 and 217.80 $HV_{0.01}$ for the samples sintered at 700 °C and 800 °C, respectively. Fig. 7 show representative P-h curves for each layer which compound the gradient structure, and Table 5 presents the retrieved information from the P-h curves. All the P-h curves show a pseudo-creep behaviour (see the plateau area of the curve) despite the short dwell time, as a result of the porosity. The Young's modulus is affected by the porosity as well, exhibiting values comprised between 44.7 and 65.9 GPa. Nonetheless, when indentations were performed in relatively fully dense zones, the achieved values for Young's modulus were of 85.7 and 98.8 GPa for the samples sintered at 700 °C and 800 °C, respectively.

Table 6 presents a summary of the estimated mechanical properties using the Nielsen method [85], Jha correlation [86], and Wu correction factors [87] for samples with radial porosity gradient and their constituent layers, obtained from the values of the porosity percentage and the pore shape factor determined by image analysis. Information is expressed in terms of the mean value ± standard error. It can be observed that the values acquired for the sample sintered at 700 °C are lower than those estimated for the sample sintered at 800 °C. Consequently, the calculated elastic modulus is 41.26 and 56.08 GPa for the samples sintered at 700 °C and 800 °C, respectively. Regarding the estimated yield stress values, they are 144 and 181 MPa for the samples sintered at 700 °C and 800 °C, respectively. These values are compared with the properties of human bone, where the Young's modulus is comprised in the range of 0.1–0.5 GPa for trabecular bone [20], and 20–25 GPa for cortical bone [67] and the yield strength is in the range of 2–12 MPa for trabecular bone [20], and 90–230 MPa for cortical bone [88]. In particular, the femoral human bone, which has a porous core and a denser outer layer [89], as the proposed porous gradient proposed in this work, has a Young's modulus of 19 GPa and a yield strength of 115 MPa [90].

Table 4
Obtained roughness parameters of the top view surface of the sintered samples.

Sintering temperature	R_a	R_q	R_c	R_z
[°C]	[μm]	[μm]	[μm]	[μm]
700	19.0 ± 0.9	25.1 ± 1.1	117.9 ± 4.7	159.7 ± 17.4
800	10.8 ± 0.7	15.0 ± 0.9	74.4 ± 3.8	109.6 ± 5.5

4. Discussion

During the sintering stage, the formation of necks confers the mechanical strength of the structure. The formation of these necks results in dimensional changes (shrinkage), which are inherent to the powder metallurgy process. Additionally, the sintering technique employed in this study (FAST/SPS) applies uniaxial pressure to the sample, which tends to increase the shrinking phenomenon. Nonetheless, the maximum shrinkage percentage found in this study is 21 % for the sample sintered

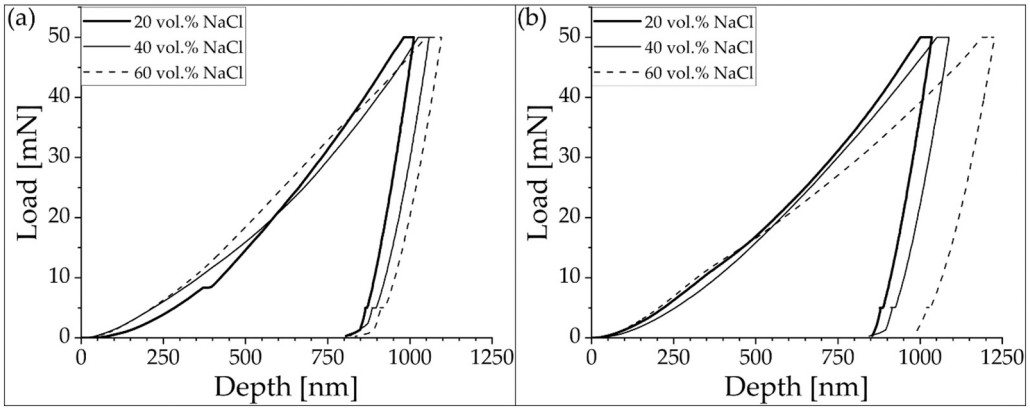

Fig. 7. Representative P-h curves at 50 mN load and 1 s of dwell time for sintered samples at: (a) 700 °C and (b) 800 °C.

Table 5
Representative values of nanoindentation measurements in each layer for the obtained samples.

Sintering temperature	Layer	Porosity	Max. penetration	Elastic recovery	Pseudo-creep
[°C]		[%]	[nm]	[nm]	[nm]
700	External	27.5 ± 4.6	1012 ± 30	158 ± 4	31 ± 2
	Intermediate	46.1 ± 1.8	1058 ± 33	160 ± 4	34 ± 2
	Internal	65.7 ± 3.7	1075 ± 37	166 ± 6	47 ± 3
800	External	18.2 ± 1.9	1035 ± 32	147 ± 5	35 ± 2
	Intermediate	42.7 ± 1.6	1088 ± 40	192 ± 6	38 ± 3
	Internal	57.5 ± 4.1	1226 ± 33	196 ± 7	41 ± 2

Table 6
Experimental ($E_{O\&P}$) and Estimated mechanical properties using the Nielsen method [84], Jha correlation [85], and Wu correction factors [86] for structures with radial gradients based on the mixing rule (ROM).

Sintering temperature	Layer	Exp.	Estimated			
		$E_{O\&P}$	$E_{Nielsen}$	$\sigma_{Y,Jha}$	E_{ROM}	$\sigma_{Y,ROM}$
[°C]		[GPa]	[GPa]	[MPa]	[GPa]	[MPa]
700	External	65.9 ± 1.3	44.1 ± 5.7	180 ± 59	41.3 ± 4.3	144 ± 15
	Intermediate	56.0 ± 1.1	19.9 ± 1.5	91 ± 7		
	Internal	52.9 ± 1.0	8.0 ± 1.9	36 ± 9		
800	External	59.2 ± 1.1	62.1 ± 3.2	229 ± 11	56.1 ± 2.7	181 ± 9
	Intermediate	54.7 ± 1.0	23.4 ± 1.6	105 ± 6		
	Internal	44.7 ± 0.9	11.4 ± 2.5	57 ± 12		
Human bone	Trabecular	–	0.1–0.5	2–12	19.0 ± 1.8*	115 ± 16*
	Cortical	–	20–25	90–230		

* Values for femoral human bone.

at 800 °C. Considering that the green sample has been sintered after the removal of the space-holder particles, this mentioned value is relatively low compared to typical shrinkages obtained by other high densification techniques, such as Hot-Isostatic Pressing, which typically range from 30 to 35 % [91]. Furthermore, it is comparable to the shrinkage obtained by other techniques such as metal injection moulding (MIM) when used with the space-holder technique, that presents a linear shrinkage ranging between 15 and 20 % [92].

Regarding the physical and microstructural characterisation of the samples, the observed porosity agglomeration at each interface can be the result of different phenomena: the quantity of space holder added in each layer, the rearrangement of the powder particles during pre-compaction, the combined effect of mechanical property discrepancies between each layer, and/or the applied pressure during the sintering process. It is worth highlighting the fact that the radially graded porosity was achieved, despite the pressure applied during sintering.

The sample configuration was meticulously devised to confer resilience upon the external, more compact layers, enabling them to withstand the compressive forces imparted during the sintering procedure. This strategic arrangement effectively prevents potential collapse within the interior, more porous layers.

According to the results obtained from the image analysis, it was determined that the porosity distribution in the three gradient zones is consistent with the amount of spacer particles used in each layer. Furthermore, regardless of the sintering temperature used, a significant amount of interconnected porosity is observed in all the zones. The higher the concentration of spacer particles, the greater the coalescence of the pores. This coalescence phenomenon results in the formation of more irregular pores. This can be seen in the core layer. Furthermore, the sintering temperature has an effect on the equivalent pore diameter, which decreases when increasing temperature. Also, lower temperatures and the concentration of spacer particles lead to higher particle coalescence, resulting in elongated defects. In particular, the temperature impact on particle diffusion is more pronounced at the internal interfaces, as the union between two highly porous layers (40 vol% and 60 vol%), as seen in the sample sintered at 700 °C (Fig. 4(e) and (e)). This represents a potential stress concentrator and a region with a high probability of structural failure. The enhanced homogeneity observed in the sample sintered at 800 °C can be attributed to the notable increase in the diffusion rate resulting from higher sintering temperatures in the FAST/SPS process, promoting better neck formation [93,94]. Conversely, the absence of elongated defects in the overall view of the sample sintered at 800 °C signifies a more reliable union.

Furthermore, rounded corners of the observed pores reduce stress concentration and decrease the probability of failure, while the roughness observed on the internal walls can be beneficial to cell adhesion and improve osseointegration [23].

Moreover, upon comparing the porosities measured by Archimedes' test, it is evident that the relative percentages of interconnected porosity compared to total porosity are 98.3 % and 97.6 % for samples sintered at 700 °C and 800 °C, respectively. These values indicate that the obtained samples present an open-cell structure, with a substantial interconnectedness of nearly all total porosity in both samples. This characteristic proves to be advantageous and highlights the potential application of

these structures as porous implants, facilitating fluid transport and promoting bone ingrowth [20,95,96]. It is observed that the porosity determined from the image analysis (*P(IA)*) has a standard deviation of approximately 5 % in both analysed cases, which encompasses the entire range of porosity obtained by Archimedes measurements (P_T). This indicates that it does not represent a significant error affecting the measurements, confirming that both methods are reliable for the determination of porosity, despite image analysis considering only the analysed surface.

Based on the comparison of means, it was determined that these differences are statistically significant ($p_{value} < 0.05$). This significant difference also extends to the total porosity of the samples, concluding that with an increase of 100 °C in sintering temperature, the total porosity of the sample is reduced by almost 10 %. This can lead to reinforcement of the porous material, allowing it to withstand higher mechanical loads before collapsing. Moreover, the mechanical bonding between Ti particles achieved during cold compaction by means of deformation and cold-welding, have allowed to withstand the pressure applied during sintering without the collapse of the structure. Hence, it was possible to utilise the minimum pressure required to ensure contact between punches and the sample during the sintering stage, thereby attaining adequate current flow for the formation of sintering necks. Furthermore, due to the sintering mechanism of the FAST/SPS technique, which operates via Joule's effect and is localized at particle contact points, lower temperatures (50–60 % of the material's melting point [97]) can be employed compared to conventional sintering methods (80–90 % of the material's melting point [98]) to achieve sintering necks. This approach allows an optimal balance between biomechanical and biofunctional behaviour in bone replacement applications. The obtained porosities, close to the design values for the sample sintered at 800 °C, demonstrate the potential of employing FAST/SPS in conjunction with the space holder technique to achieve structures with desired porosity percentages or tailor-maid design without the need for specialised tools.

It is essential to consider that due to the dimensions of the outer layer of each sample, which corresponds to 51 % of the total sample volume, this region contributes the most to the pore count. As a result, the mean equivalent pore diameter for the entire sample tends to resemble the mean equivalent pore diameter of the outer layer.

Furthermore, in the literature, it has been reported that cell migration may be limited in small-sized pores, and cell adhesion may be affected by pore size [77]. In this regard, Akay et al. [99] observed that in 40 μm pores, there was higher cell viability, and cell migration occurred more rapidly than in 100 μm pores. Nonetheless, these sizes were not effective for cellular penetration or mineralisation. This highlights the importance of the inherent porosity in the powder metallurgy manufacturing route, which needs to be accompanied by a larger-sized porosity to achieve synergy that enhances the biological performance of the structure. Additionally, it has been reported that porosity with sizes ranging from 100 to 300 μm allows for cellular penetration, migration, growth, as well as optimal tissue vascularization [75]. On the other hand, larger-sized pores facilitate the transport of oxygen and nutrients into the scaffold, aiding in better integration between the bone and the implant [100]. However, large pores provide a low rate of bone ingrowth, this is due to the fact that at early stages of bone formation only a small amount of bone fills the implant pores, which results in more empty spaces in large porosities compared to small porosities [100]. In addition, the stress concentration in porous Ti samples increases with pore size and decreases with pore distance, due to the stress field interactions between the pores [101]. While no clear consensus has emerged yet regarding the optimal pore size for bone ingrowth, interconnected pore structure with pore sizes between 50 and 300 μm provides a suitable environment for osseointegration and osseoconduction, which improves bone implant fixation [102,103]. Nonetheless, the appropriate pore size for bone regeneration is still not well defined due to the different advantages that can provide small pores as well as large pores [104–106]. For this reason, the use of structures with porosity gradients is attractive to allow all the necessary enhancement in biological activity that leads to proper bone growth, highlighting the relevance of the porosity distributions obtained in both samples.

The fact that the pore size in the inner layers is larger than that in the outer layers is mainly due to the amount of spacer added. Having a greater amount of spacer particles in the inner layer increases the probability of two spacer particles coming together and forming a much larger pore. Besides, statistically significant differences are found in the equivalent pore diameters in each layer, when employing a sintering temperature of 800 °C. Nevertheless, in accordance with the requirements for good biological performance of porous structures, the equivalent pore diameters found with both sintering temperatures fall within the recommended pore size ranges. Thus, the difference found mainly corresponds to a higher densification of the structure as a result of the greater diffusion resulting from the use of a higher temperature during the sintering process [66].

The pore shape factor (F_f) describes the aspect ratio of the pores. An F_f value of 1 indicates a round pore, while a value close to 0 indicates a needle-shaped pore. The shape of the pores plays a decisive role in cell growth. In this regard, Bidan et al. [107] observed that by optimising the shape of the pores, the rate of growth of bone tissue in the porous structure can be increased, with cells tending to grow faster in square pores ($F_f = 0.78$) without convexities. In this work, the values are close to those reported by Bidan et al. [107] for square pores, which is consistent with the polygonal morphology of the spacer particles used. On the other hand, the shape factor values obtained in the inner layer of both samples may result from the agglomeration of spacer particles, which tend to form elongated pores when they come together. The shape factor values increase in the intermediate layers and reach their maximum values in the external layer, reinforcing the criterion that pore agglomeration reduces the shape factor value.

Upon comparing the pore shape factor values, there is indeed a significant difference observed in statistical terms ($p_{value} < 0.05$) between samples sintered at different temperatures. Nevertheless, this difference does not dramatically affect the mechanical performance of the structure since the pores are not elongated, which could cause an anisotropic behaviour.

The pore distance (λ) allows to determine the average spacing between pores. Two types of pore distances were measured in this study: (i) the distance between micropores (λ_{pm}), which are formed during the manufacturing process of metal powders, and (ii) the distance between macropores (λ_{sh}), which are induced by the addition of spacer particles. Regarding the micropore values obtained, it is noteworthy noting that they are smaller than the sizes of the metal powder particles used. Therefore, they do not correspond to the detachment of particles resulting from poor sintering, but rather to the unfilled interstices due to the morphology of the metal powders during compaction. Notwithstanding, the difference between the ranges of macropore distances confirms that higher densification was achieved at sintering temperatures of 800 °C, which is consistent with the porosity values and equivalent pore diameter. The increased spacing between pores contributes to a stiffer structure, with the outer layer having the highest distances and being responsible for supporting the mechanical stresses [101].

Apart from porosity, surface roughness can also impact the interaction between bone and the implant, potentially affecting adhesion, growth, proliferation, and differentiation of osteoblastic cells [108]. In this study, the obtained R_a values exceed the commonly studied threshold (<5 μm) for assessing the effect of roughness on cell behaviour [109]. However, previous research by Ponader et al. [110] showed that if R_a is below 25 μm, surface roughness has a positive effect on the differentiation and proliferation of human osteoblast cells, while R_a values above 57 μm have negative effects. Additionally, Shaoki et al. [111] found through in vivo studies that implants with rough surface ($R_a = 10.65$ μm; $R_q = 13.05$ μm) tend to exhibit greater cell adhesion and

differentiation compared to implants with smoother surfaces ($R_a = 0.33$ μm; $R_q = 0.43$ μm). Therefore, it can be observed that the sample sintered at 800 °C has R_a y R_q values similar to those in the study by Shaoki et al. [111], whereas both samples have $R_a < 25$ μm roughness values, indicating a potential positive effect on cell differentiation and proliferation in in vitro or in vivo studies. The values of R_c and R_z provide insights into the depth of the pores. For instance, Tsukanaka et al. [112] reported porous Ti structures manufactured by Selective Laser Melting (SLM) with R_z values around 150 μm, which did not have specific effects on osteoblastic differentiation compared to flat-rolled Ti surfaces. Hence, it can be expected that the values obtained in this study would also not have negative effects on cell behaviour.

In terms of mechanical characterisation of the sintered samples, the microhardness values obtained for both samples are lower than the average microhardness value of Ti grade 4 (301 HV). This can be attributed to the presence of microporosity, as the indentations made on the analysed surfaces have diagonal lengths of 10.41 ± 1.85 μm and 9.93 ± 1.84 μm for the samples sintered at 700 °C and 800 °C, respectively, which are very close to the reported micropore distances (λ_{pm}). To mitigate the interference of porosity with hardness measurements, nanoindentation analysis was performed, where the achieved values are higher than those reported by Ertoter et al. [113] for bulk samples with a bimodal nanocrystalline structure of Ti c.p., manufactured by SPS. The nanoindentation values also fall within the hardness range reported by Chaudhari & Bauri [114] for bulk samples of Ti c.p. produced by SPS. Moreover, the range of the elastic modulus for the sample sintered at 800 °C includes the elastic modulus value of pure titanium (110 GPa), indicating that the sintering temperature was sufficient to adequately consolidate the metallic powders, which aligns with the observations made in optical microscopy and SEM images.

As expected, the representative P-h curves presented for each layer of the gradient show a direct effect of the porosity level on the achieved mechanical properties. Each curve shows a pseudo-creep behaviour, which is higher when the porosity level is increased. This effect is related to the mean free path of the samples; i.e. when the distance between two pores (λ) is high enough, the porous titanium substrate will behave close to the fully dense c.p. Ti [115]. Comparing the mechanical properties estimated from the nanoindentation measurements with the calculated ones by means of Nielsen's equation, it can be seen a similar behaviour when comparing the different layers which comprises the gradient structure. As expected, the nanoindentation measurements have reached higher values due to the scale, but permit to validate the ones obtained by means of mathematical expressions.

The obtained mechanical property values are those expected owing to the higher degree of porosity and lower elastic modulus achieved at the lower temperature. Furthermore, the internal layers exhibit significantly lower properties compared to the external layers, which can be attributed to the porosity distribution. Since the volumetric fraction of the structures is higher in the layers with less porosity, the estimated mechanical properties for the entire sample are similar to those of the denser layers. Additionally, the estimated Young's modulus values are closer to the value of cortical bone's Young's modulus (approximately 30 GPa), which helps mitigate the stress shielding phenomenon, a persistent issue in the development of structures for bone replacement [21,67].

Nonetheless, the bones of the adult skeleton are composed by two regions that display different architectures [116]: (i) the outer region is formed by cortical bone which exhibits a porosity that ranges 5–15 vol %, and (ii) the inner region, formed by trabecular bone that has porosity in the range of 40–95 vol% [117]. The porosity level affect directly the mechanical properties of each bone: cortical bone can withstand stress up to 150 MPa, and has an elastic modulus up to 30 GPa, while trabecular bone can withstand stress up to 50 MPa and exhibits an elastic modulus up to 10 GPa [104]. In this sense, each layer of the produced structures mimics the hierarchical structure of the bone. In one hand, the inner layer reached yield strength in the range of 36–57 MPa with an elastic modulus of 8–11 GPa is comparable to the trabecular bone. On the other hand, the outer layer reached yield strength in the range of 180–229 MPa and an elastic modulus of 44–62 GPa, meeting the mechanical requirements of cortical bone. The intermediate layer provides additional mechanical resistance to enhance the behaviour of the inner layer while smoothly changes the porosity from 60 vol % at the inner layer to 20 vol% at the outer layer.

In the case of the estimated yield stress values, it is crucial for them to be close to that of cortical bone (approximately 180 MPa) in order to fulfil the intended function for which these structures are designed [21,67]. In this regard, it can be observed that only the sample sintered at 800 °C meets the design requirements for the intended application. Nonetheless, it can be stated that the mechanical behaviour will be enhanced when the osseointegration of the implant is completed, due to the fact that the new formed bone will fill the pores conferring more mechanical strength [41]. Also, it is important to remark that when sintering at high temperature (800 °C), the interfaces between layers are homogeneous improving the mechanical integrity, which in combination with a denser outer layer may help to enhance the fatigue behaviour of the proposed structure [74]. Torres et al. [67] reported titanium structures with a radial porosity gradient fabricated using conventional powder metallurgy, which exhibited an elastic modulus of 8.3 GPa and a yield stress of 278 MPa. Nevertheless, these structures had an inverse porosity gradient compared to the one presented in this work, where the denser layer is located inside the structure while the more porous layer is on the outside. Since the layers have different volumetric fractions, which directly influence the mechanical properties of the structure, direct comparison of the results is not possible. One notable difference between the fabrication of these two structures is the processing time: using SPS, the sintering time was 5 min at 800 °C, whereas conventional sintering takes place for 2 h at 1250 °C [67] (0.5 h vs. 24 h of cycle time).

To the best of our knowledge, the manufacturing of titanium structures with radial porosity gradient using the Spark Plasma Sintering (SPS) technique has not been reported to date. Baghtifouni et al. [74] successfully fabricated titanium structures with longitudinal porosity gradient using SPS. In their work, a sintering temperature of 440 °C with a sintering time of 8 min was used, and various combinations of porosity were tested. Only the structure with layers of porosity of 30/60/70/60/30 vol% NaCl exhibited the required yield strength for bone tissue replacement applications. The failure mode in their work determined that structures with a longitudinal porosity gradient withstand higher mechanical stresses, because cracks change direction when transitioning from one layer to another, thus delaying failure. However, the provided images did not show the interfaces that would allow verification of the bonding quality between layers. Therefore, the sintering temperature (440 °C) might have been a limitation in achieving larger samples with better mechanical properties.

In another study, Zhang et al. [73] fabricated porous titanium samples by means of SPS, using NH_4HCO_3 as spacer particles and a specially designed matrix to avoid applying pressure to the sample, while keeping sintering temperatures ranging from 1000 to 1200 °C during 5 min. They successfully obtained induced porosity with the spacers, with micropores of 20 μm. In this study, a sintering temperature lower than that employed by Zhang et al. [73], but higher than that used by Baghtifouni et al. [74], was achieved, thanks to no temperature limitation given by NaCl as a spacer due to it was removed before sintering, while obtaining good porosity control without the need for a matrix to avoid pressure application. For its part, Li et al. [49] fabricated gradient structures with radial porosity by Laser Powder Bed Fusion (LPBF); elastic moduli <20GPa were obtained, however the fatigue life of the material was insufficient, the pore morphology obtained facilitated crack initiation. Thus, the study of these structures is planned to be extended to determine their actual mechanical and fatigue behaviour, as fatigue is one of the main mechanical failures of implants [21], in addition to studying their biological behaviour.

5. Conclusions

In this study, Ti grade 4 samples with a radially graded porous structure were successfully fabricated using FAST/SPS combined with space holder technique utilising NaCl as spacer particles. The influence of temperature on porosity and mechanical properties was leading to the following conclusions:

- The FAST/SPS processing route, combined with the spacer technique, proved highly effective in producing tailor-made titanium samples with a radial porosity gradient. This technique eliminates the need for a matrix to prevent pressure application during sintering. By sintering these samples at 800 °C for 5 min under a pressure of 6.3 MPa, interconnected porosity is achieved, maintaining the desired porosity percentage induced by the spacer particles.
- The sizes and morphology of both macro and micropores, as well as the resulting roughness values, fall within the appropriate ranges for ensuring cell viability, adhesion, and proliferation. These structures exhibit significant potential for utilisation in bone replacement applications.
- Sintering the samples at 800 °C yields results in more uniform interfaces, effectively reducing stress concentration effects. Furthermore, each layer contributes to the overall structure's mechanical properties, achieving in a yield stress of 181 MPa and an elastic modulus of 56GPa. These mechanical properties make the structure a viable candidate for replacing human long bones, meeting the required standards for yield stress ($\sigma_y \approx 180$ MPa) and elastic modulus (approximately 30 GPa) while having a hierarchical structure that mimics the natural bone.

CRediT authorship contribution statement

The manuscript was written through contributions of all authors. All authors have given approval to the final version of the manuscript. Ricardo Chávez-Vásconez: Conceptualization, Methodology, Investigation, Validation, Formal analysis and Writing- Original Draft; Daniel Auger-Solís: Investigation and Formal Analysis; Eva M. Pérez-Soriano: Writing - Original Draft; Writing - Review & Editing; Cristina Arévalo: Methodology, Formal analysis, Writing- Review & Editing, Supervision; Isabel Montealegre: Formal analysis, Writing- Review & Editing; Javiera Valencia-Valderrama: Investigation and Writing- Original Draft; Mauricio Reyes-Valenzuela: Investigation and Formal analysis, Supervision; Carolina Parra: Writing- Review & Editing and Funding acquisition; Rodrigo Segura-del Río: Resources and Investigation; Yadir Torres: Conceptualization, Formal analysis, Writing- Review & Editing, Sheila Lascano: Conceptualization, Methodology, Formal Analysis, Investigation, Resources, Writing- Review & Editing, Visualization, Supervising, Funding acquisition and Project administration.

Funding sources

This work was supported by the Agencia Nacional de Investigación y Desarrollo (ANID) of Chile government [FONDECYT 1231834, FONDEQUIP EQM170156, EQM190179 and EQM170220, Scholarship Program/DOCTORADO/2021-21211274], the funding of Dirección General de Investigación, Innovación y Emprendimiento of Universidad Técnica Federico Santa María - Chile [grant number USM PI-M-2022-04], and R + D + i project PDC2022-13339-I00, founded by MCIN/AEI/10.13039/501100011033/.

Declaration of competing interest

The authors declare that they have no known competing financial interests or personal relationships that could have appeared to influence the work reported in this paper.

Data availability

The raw and processed data requested to replicate these results cannot be made available at this time, as they are also part of an in-progress research study.

Acknowledgement

The authors thank the laboratory technicians Jesús Pinto at Universidad de Sevilla (Spain), Claudio Aravena and Gabriel Cornejo at Universidad Técnica Federico Santa María (Chile) for their support carrying out the microstructure characterisation and mechanical testing, Dr. Claudio Garcia at Universidad de Santiago (Chile) for his support to perform nanoindentation tests, and Bárbara Arce at Universidad Técnica Federico Santa María (Chile) for the design of the graphical abstract.

References

[1] Cauley JA, Chalhoub D, Kassem AM, Fuleihan GE-H. Geographic and ethnic disparities in osteoporotic fractures. Nat Rev Endocrinol 2014;10:338.
[2] Torres Y, Hernández GB, Nieto I, Pavón JJ, Lascano S, Rodríguez JA. Processing and characterization of porous titanium by using NaCl as space holder. In: Amigó V, editor. III Congreso Nacional de Pulvimetalurgia. Valencia, Spain: Universitat Politècnica de València; 2010. p. 455–68.
[3] https://www.vitamk7.com/bone_health.php, BONE HEALTH, in.
[4] Brown MA, Duncan EL. Genetic studies of osteoporosis. Expert Rev Mol Med 1999;1:1–18.
[5] Torres Y, Pavón JJ, Nieto I, Rodríguez JA. Conventional powder metallurgy process and characterization of porous titanium for biomedical applications. Metall Mater Trans B 2011;42:891–900.
[6] https://www.populationpyramid.net/chile/2050/, Population Pyramids of the World from 1950 to 2100, in.
[7] Desa U, United Nations Department of Economic and Social Affairs, Population Division. World population prospects: the 2015 revision, key findings and advance tables. In: Technical report: working paper no. ESA/P/WP. 241; 2015.
[8] U. Nations. Department of economic and social affairs, population division. In: World population ageing 2015 (ST/ESA/SER.A/390). New York: UN; 2015.
[9] Cooper C, Campion G, Melton LR. Hip fractures in the elderly: a world-wide projection. Osteoporos Int 1992;2:285–9.
[10] Gänsslen A, Gösling T, Hildebrand F, Pape H, Oestern H. Femoral shaft fractures in adults: treatment options and controversies. Acta Chir Orthop Traumatol Cech 2014;81:108.
[11] Data G. Global dental implant devices market forecast (US$nb). 2018–2018.
[12] https://www.dentistasalcantara.cl/implantes-dentales/, Implantes Dentales, in.
[13] Amin S, Achenbach SJ, Atkinson EJ, Khosla S, Melton III LJ. Trends in fracture incidence: a population-based study over 20 years. J Bone Miner Res 2014;29:581–9.
[14] Wright NC, Saag KG, Curtis JR, Smith WK, Kilgore ML, Morrisey MA, et al. Recent trends in hip fracture rates by race/ethnicity among older US adults. J Bone Miner Res 2012;27:2325–32.
[15] Ritchie RO. Role of fracture mechanics in life prediction and quality control of medical implants. In: ASM Intl. Materials and processes for medical devices conference, St. Minnesota: Paul; 2004.
[16] Kaur M, Singh K. Review on titanium and titanium based alloys as biomaterials for orthopaedic applications. Mater Sci Eng C 2019;102:844–62.
[17] Singh R, Lee PD, Dashwood RJ, Lindley TC. Titanium foams for biomedical applications: a review. Mater Technol 2010;25:127–36.
[18] Niinomi M, Nakai M, Hieda J. Development of new metallic alloys for biomedical applications. Acta Biomater 2012;8:3888–903.
[19] Schmidutz F, Agarwal Y, Müller PE, Gueorguiev B, Richards RG, Sprecher CM. Stress-shielding induced bone remodeling in cementless shoulder resurfacing arthroplasty: a finite element analysis and in vivo results. J Biomech 2014;47:3509–16.
[20] Lascano S, Chávez-Vásconez R, Muñoz-Rojas D, Aristizabal J, Arce B, Parra C, et al. Graphene-coated Ti-Nb-Ta-Mn foams: a promising approach towards a suitable biomaterial for bone replacement. Surf Coat Technol 2020;401:126250.
[21] Chávez-Vásconez R, Lascano S, Sauceda S, Reyes-Valenzuela M, Salvo C, Mangalaraja RV, et al. Effect of the processing parameters on the porosity and mechanical behavior of titanium samples with bimodal microstructure produced via hot pressing 2022;15:136.
[22] R. Chávez-Vásconez, C. Arévalo, Y. Torres, M. Reyes-Valenzuela, S. Sauceda, C. Salvo, R.V. Mangalaraja, I. Montealegre, E.M. Perez-Soriano, S.J. Lascano, Understanding the synergetic effects of mechanical milling and hot pressing on bimodal microstructure and tribo-mechanical behavior in porous Ti structures, (2023).
[23] C. Song, L. Liu, Z. Deng, H. Lei, F. Yuan, Y. Yang, Y. Li, J.J. Yu, Research progress on the design and performance of porous titanium alloy bone implants, (2023).
[24] Wenjuan N, Chenguang B, GuiBao Q, Qiang W. Processing and properties of porous titanium using space holder technique. Mater Sci Eng A 2009;506:148–51.

[25] Kashef S, Asgari A, Hilditch TB, Yan W, Goel VK, Hodgson PD. Fatigue crack growth behavior of titanium foams for medical applications. Mater Sci Eng A 2011;528:1602–7.
[26] Torres Y, Rodríguez JA, Arias S, Echeverry M, Robledo S, Amigó V, et al. Processing, characterization and biological testing of porous titanium obtained by space-holder technique. J Mater Sci 2012;47:6565–76.
[27] Civantos A, Giner M, Trueba P, Lascano S, Montoya-García M-J, Arévalo C, et al. In vitro bone cell behavior on porous titanium samples: influence of porosity by loose sintering and space holder techniques. Metals 2020;10:696.
[28] Zhao YY, Fung T, Zhang LP, Zhang FL. Lost carbonate sintering process for manufacturing metal foams. Scr Mater 2005;52:295–8.
[29] Manonukul A, Muenya N, Léaux F, Amaranan S. Effects of replacing metal powder with powder space holder on metal foam produced by metal injection moulding. J Mater Process Technol 2010;210:529–35.
[30] Fengqiu T, Fudouzi H, Uchikoshi T, Sakka Y. Preparation of porous materials with controlled pore size and porosity. J Eur Ceram Soc 2004;24:341–4.
[31] Guden M, Celik E, Akar E, Cetiner S. Compression testing of a sintered Ti6Al4V powder compact for biomedical applications. Mater Charact 2005;54:399–408.
[32] Torres Y, Pavón JJ, Rodríguez JA. Processing and characterization of porous titanium for implants by using NaCl as space holder. J Mater Process Technol 2012;212:1061–9.
[33] Dunand D. Processing of titanium foams. Adv Eng Mater 2004;6:369–73.
[34] Torres Y, Lascano S, Bris J, Pavón J, Rodriguez JA. Development of porous titanium for biomedical applications: a comparison between loose sintering and space-holder techniques. Mater Sci Eng C 2014;37:148–55.
[35] Fujii T, Murakami R, Kobayashi N, Tohgo K, Shimamura Y. Uniform porous and functionally graded porous titanium fabricated via space holder technique with spark plasma sintering for biomedical applications. Adv Powder Technol 2022;33:103598.
[36] Torres Y, Pavón J, Trueba P, Cobos J, Rodriguez-Ortiz JA. Design, fabrication and characterization of titanium with graded porosity by using space-holder technique, Procedia. Mater Sci 2014;4:115–9.
[37] Lascano S, Arévalo C, Montealegre-Melendez I, Muñoz S, Rodriguez-Ortiz JA, Trueba P, et al. Porous titanium for biomedical applications: evaluation of the conventional powder metallurgy frontier and space-holder technique. Appl Sci 2019;9:982.
[38] Abbasi N, Hamlet S, Love RM, Nguyen N-T. Porous scaffolds for bone regeneration. J Sci Adv Mater Devices 2020;5:1–9.
[39] Zhang Y, Wang J. Fabrication of functionally graded porous polymer structures using thermal bonding lamination techniques. Procedia Manuf 2017;10:866–75.
[40] Dubey A, Jaiswal S, Lahiri D. Promises of functionally graded material in bone regeneration: current trends. properties, and challenges, ACS Biomater Sci Eng 2022;8:1001–27.
[41] A. Pattnaik, A.S. Sanket, S. Pradhan, R. Sahoo, S. Das, S. Pany, T.E. Douglas, R. Dandela, Q. Liu, J.J.B. Rajadas, Designing of gradient scaffolds and their applications in tissue regeneration, (2023) 122078.
[42] Wang S, Zhou X, Liu L, Shi ZA, Hao Y. On the design and properties of porous femoral stems with adjustable stiffness gradient. Med Eng Phys 2020;81:30–8.
[43] Liu B, Wang H, Zhang N, Zhang M, Cheng C-K. Femoral stems with porous lattice structures: a review 2021;9.
[44] McKay WF. Reinforced porous spinal implants, in. Google Patents. 1997.
[45] Mehrali M, Shirazi FS, Mehrali M, Metselaar HSC, Kadri NAB, Osman NAA. Dental implants from functionally graded materials. J Biomed Mater Res A 2013;101:3046–57.
[46] Li Y, Feng Z, Hao L, Huang L, Xin C, Wang Y, et al. A review on functionally graded materials and structures via additive manufacturing: from multi-scale design to versatile functional properties. Adv Mater Technol 2020;5:1900981.
[47] Xiong Y, Han Z, Qin J, Dong L, Zhang H, Wang Y, et al. Effects of porosity gradient pattern on mechanical performance of additive manufactured Ti-6Al-4V functionally graded porous structure. Mater Des 2021;208:109911.
[48] Xu W, Yu A, Jiang Y, Li Y, Zhang C, Singh H-p, Liu B, Hou C, Zhang Y, Tian S, Zhang J, Lu X. Gyroid-based functionally graded porous titanium scaffolds for dental application: design, simulation and characterizations. Mater Des. 2022;224:111300.
[49] Li Z, Chuzenji M, Mizutani, E. A MJMS. Compression and fatigue performance of Ti6Al4V materials with different uniform and gradient porous structures. Mater Sci Eng A 2023;873:145030.
[50] Song C, Liu L, Deng Z, Lei H, Yuan F, Yang Y, et al. Research progress on the design and performance of porous titanium alloy bone implants. J Mater Res Technol 2023;23:2626–41.
[51] Tüzemen MÇ, Salamcı E, R.J.J.o.M.P.. Ünal, Additive manufacturing design approach to strut-based functionally graded porous structures for personalized implants 2022;84:1526–40.
[52] Parthasarathy J, Starly B, Raman S, Christensen A. Mechanical evaluation of porous titanium (Ti6Al4V) structures with electron beam melting (EBM). J Mech Behav Biomed Mater 2010;3:249–59.
[53] Oppenheimer SM, Dunand DC. Porous NiTi by creep expansion of argon-filled pores. Mater Sci Eng A 2009;523:70–6.
[54] Zhou L, Yuan T, Tang J, He J, Li R. Mechanical and corrosion behavior of titanium alloys additively manufactured by selective laser melting – a comparison between nearly β titanium, α titanium and α + β titanium. Opt Laser Technol 2019;119:105625.
[55] Orrù R, Licheri R, Locci AM, Cincotti A, Cao G. Consolidation/synthesis of materials by electric current activated/assisted sintering. Mater Sci Eng R Rep 2009;63:127–287.
[56] Esen Z, Bor ET. Characterization of loose powder sintered porous titanium and Ti6Al4V alloy. Turk J Eng Environ Sci 2009;33:207–19.
[57] Chang S, Doremus RH, Schadler LS, Siegel RW. Hot-pressing of nano-size alumina powder and the resulting mechanical properties. Int J Appl Ceram Technol 2004;1:172–9.
[58] Yang C, Ni S, Liu Y, Song M. Effects of sintering parameters on the hardness and microstructures of bulk bimodal titanium. Mater Sci Eng A 2015;625:264–70.
[59] Lopez EIP, Saint-Laurence PIM, Ramirez CEA, Gomez LB, Flores AM, Jimenez FDLC, et al. Estudio de perfiles de difracción de rayos X de una aleación Ti-13Ta-3Sn obtenida por aleado mecánico. Matéria 2020;25.
[60] Riaz A, Polley C, Lund H, Springer A, Seitz H. A novel approach to fabricate load-bearing Ti6Al4V-Barium titanate piezoelectric bone scaffolds by coupling electron beam melting and field-assisted sintering. Mater Des 2023;225:111428.
[61] Derakhshani B, Parvin N, Khodaei M. Influence of sintering temperature on the mechanical properties and biocompatibility of titanium-nano hydroxyapatite functionally graded materials. J Mater Res Technol 2023;27:2538–47.
[62] Kashimbetova A, Slámečka K, Díaz-de-la-Torre S, Méndez-García JC, Hernández-Morales B, Piña-Barba MC, et al. Pressure-less spark plasma sintering of 3D-plotted titanium porous structures. J Mater Res Technol 2023;22:2147–57.
[63] Radajewski M, Decker S, Krüger L. Direct temperature measurement via thermocouples within an SPS/FAST graphite tool. Measurement 2019;147:106863.
[64] Ratzker B, Sokol M. Exploring the capabilities of high-pressure spark plasma sintering (HPSPS): a review of materials processing and properties. Mater Des 2023;112238.
[65] Hu Z-Y, Zhang Z-H, Cheng X-W, Wang F-C, Zhang Y-F, Li S-L. A review of multi-physical fields induced phenomena and effects in spark plasma sintering: fundamentals and applications. Mater Des 2020;191:108662.
[66] Maharana S, Prasad DKVD, Seetharaman SA, Sabat M, Laha T. Effect of sintering parameters on phase evolution, microstructural development and mechanical behavior of Ni46Al12Co18Cr8Fe12Mo4 high entropy alloy synthesized via mechanical alloying and spark plasma sintering. Mater Sci Eng A 2023;886:145695.
[67] Torres Y, Trueba P, Pavón JJ, Chicardi E, Kamm P, García-Moreno F, et al. Design, processing and characterization of titanium with radial graded porosity for bone implants. Mater Des 2016;110:179–87.
[68] Rodríguez-Ortiz JA, Trueba P, Torres Y, Pavón JJ. Dispositivo de compactación de polvos para obtener piezas sinterizadas con porosidad gradiante radial, procedimiento de obtención y uso. España: U.d. Sevilla; 2018. p. 24.
[69] Trueba P, Chicardi E, Rodríguez-Ortiz JA, Torres Y. Development and implementation of a sequential compaction device to obtain radial graded porosity cylinders. J Manuf Process 2020;50:142–53.
[70] Torres Y, García-Ostos C, Arévalo C, Gotor FJ, Pavón JJ, Trueba P, et al. Processing and characterization of surrogate nuclear materials with controlled radial porosity. J Nucl Sci Technol 2017;54:167–73.
[71] García-Ostos C, Rodríguez-Ortiz JA, Arévalo C, Cobos J, Gotor FJ, Torres Y. Fabrication and characterization of CeO2 pellets for simulation of nuclear fuel. Nucl Eng Des 2016;298:160–7.
[72] Yılmaz E, Kabataş F, Gökçe A, Fındık F. Production and characterization of a bone-like porous Ti/Ti-hydroxyapatite functionally graded material. J Mater Eng Perform 2020;29:6455–67.
[73] Zhang L, Zhang YQ, Jiang YH, Zhou R. Mechanical behaviors of porous Ti with high porosity and large pore size prepared by one-step spark plasma sintering technique. Vacuum 2015;122:187–94.
[74] Baghtifouni EK, Monazzah AH. Longitudinal graded porous titanium fabricated by spark plasma sintering: design of layers, direction of crack path. J Manuf Process 2022;81:738–47.
[75] Jang J-W, Min K-E, Kim C, Shin J, Lee J, Yi S. Review: scaffold characteristics, fabrication methods, and biomaterials for the bone tissue engineering. Int J Precis Eng Manuf 2023;24:511–29.
[76] ASTM E11-20.. Standard specification for woven wire test sieve cloth and test sieves, in. West Conshohocken, PA: ASTM International; 2020.
[77] Murphy CM, Haugh MG, O'Brien FJ. The effect of mean pore size on cell attachment, proliferation and migration in collagen–glycosaminoglycan scaffolds for bone tissue engineering. Biomaterials 2010;31:461–6.
[78] ASTM F1877-16.. Standard practice for characterization of particles, in. West Conshohocken, PA: ASTM International; 2016.
[79] ISO 13314:2011. Mechanical testing of metals - ductility testing - compression test for porous and cellular metals. ISO; 2011.
[80] ASTM E9-19.. Standard test methods of compression testing of metallic materials at room temperature, in. West Conshohocken, PA: ASTM International; 2019.
[81] ASTM B962-17.. Standard test methods for density of compacted or sintered powder metallurgy (PM). In: Products using Archimedes' principle. West Conshohocken, PA: ASTM International; 2017.
[82] ASTM E3-11.. Standard guide for preparation of metallographic specimens. West Conshohocken, PA: ASTM International; 2017.
[83] ISO 4287:1997. Geometrical product specifications (GPS) - surface texture: profile method - terms, definitions and surface texture parameters. ISO; 1997.
[84] Oliver WC, Pharr GM. An improved technique for determining hardness and elastic modulus using load and displacement sensing indentation experiments. J Mater Res 1992;7:1564–83.
[85] Nielsen LF. Elasticity and damping of porous materials and impregnated materials. J Am Ceram Soc 1984;67:93–8.
[86] Jha N, Mondal DP, Majumdar JD, Badkul A, Jha AK, Khare AK. Highly porous open cell Ti-foam using NaCl as temporary space holder through powder metallurgy route. Mater Des 2013;47:810–9.

[87] Wu YC, Kuo CN, Wu TH, Liu TY, Chen YW, Guo XH, et al. Empirical rule for predicting mechanical properties of Ti-6Al-4V bone implants with radial-gradient porosity bionic structures. Mater Today Commun 2021;27:102346.
[88] de Ulloa JL, González JE, Beltrán AM, Avés EP, Rodríguez-Guerra J, Torres Y. Biomechanical behavior of customized scaffolds: a three-dimensional finite element analysis. Mater Des 2022;223:111173.
[89] Lundeen GA, Knecht SL, Vajda EG, Bloebaum RD, Hofmann AA. The contribution of cortical and cancellous bone to dual-energy X-ray absorptiometry measurements in the female proximal femur. Osteoporos Int 2001;12:192–8.
[90] Mirzaali MJ, Schwiedrzik JJ, Thaiwichai S, Best JP, Michler J, Zysset PK, et al. Mechanical properties of cortical bone and their relationships with age, gender, composition and microindentation properties in the elderly. Bone 2016;93:196–211.
[91] Samarov V, Seliverstov D, Froes FH. 18 - Fabrication of near-net-shape cost-effective titanium components by use of prealloyed powders and hot isostatic pressing. In: Qian M, Froes FH, editors. Titanium powder metallurgy. Boston: Butterworth-Heinemann; 2015. p. 313–36.
[92] Neto FC, Giaretton MV, Neves GO, Aguilar C, Tramontin Souza M, Binder C, et al. An overview of highly porous titanium processed via metal injection molding in combination with the space holder method 2022;12:783.
[93] Alhazaa A, Assaifan A, Hezam M, Shar MA, Umeda J, Kondoh K. Effect of sintering temperature on the microstructure and mechanical properties of the Ti-2.5Zr alloy. Mater Res Express 2021;8:016522.
[94] Makena IM, Shongwe MB, Machaka R, Masete MS. Effect of spark plasma sintering temperature on the pore characteristics, porosity and compression strength of porous titanium foams. SN Appl Sci 2020;2:516.
[95] Mitsak AG, Kemppainen JM, Harris MT, Hollister SJ. Effect of polycaprolactone scaffold permeability on bone regeneration in vivo. Tissue Eng Part A 2011;17:1831–9.
[96] Vo TN, Kasper FK, Mikos AG. Strategies for controlled delivery of growth factors and cells for bone regeneration. Adv Drug Deliv Rev 2012;64:1292–309.
[97] Tokita M. Progress of spark plasma sintering (SPS) method. systems, ceramics applications and industrialization 2021;4:160–98.
[98] Liu PS, Chen GF. Chapter two - making porous metals. In: Liu PS, Chen GF, editors. Porous materials. Boston: Butterworth-Heinemann; 2014. p. 21–112.
[99] Akay G, Birch MA, Bokhari MA. Microcellular polyHIPE polymer supports osteoblast growth and bone formation in vitro. Biomaterials 2004;25:3991–4000.
[100] Farazin A, Zhang C, Gheisizadeh A, Shahbazi A. 3D bio-printing for use as bone replacement tissues: a review of biomedical application. Biomed Eng Adv 2023;5:100075.
[101] Zhao JH, Xie ZL, Zhong T, Sun T, Fezzaa K, Cai Y, et al. Strain rate effects on the mechanical behavior of porous titanium with different pore sizes. Mater Sci Eng A 2021;821:141593.
[102] Wang X, Nyman JS, Dong X, Leng H, Reyes M. Fundamental biomechanics in bone tissue engineering, Synthesis Lectures on. Tissue Eng 2010;2:1–225.
[103] Bansiddhi A, Dunand DC. Shape-memory NiTi foams produced by replication of NaCl space-holders. Acta Biomater 2008;4:1996–2007.
[104] Ai C, Liu L, Goh JC-H. Pore size modulates in vitro osteogenesis of bone marrow mesenchymal stem cells in fibronectin/gelatin coated silk fibroin scaffolds. Mater Sci Eng C 2021;124:112088.
[105] Porrelli D, Abrami M, Pelizzo P, Formentin C, Ratti C, Turco G, et al. Trabecular bone porosity and pore size distribution in osteoporotic patients – a low field nuclear magnetic resonance and microcomputed tomography investigation. J Mech Behav Biomed Mater 2022;125:104933.
[106] Wang X, Xu S, Zhou S, Xu W, Leary M, Choong P, et al. Topological design and additive manufacturing of porous metals for bone scaffolds and orthopaedic implants: a review. Biomaterials 2016;83:127–41.
[107] Bidan CM, Kommareddy KP, Rumpler M, Kollmannsberger P, Fratzl P, Dunlop JWC. Geometry as a factor for tissue growth: towards shape optimization of tissue engineering scaffolds. Adv Healthc Mater 2013;2:186–94.
[108] Le Guehennec L, Lopez-Heredia M-A, Enkel B, Weiss P, Amouriq Y, Layrolle P. Osteoblastic cell behaviour on different titanium implant surfaces. Acta Biomater 2008;4:535–43.
[109] Tardelli J Dias Corpa, Firmino AC Duarte, Ferreira I, dos Reis A Cândido. Influence of the roughness of dental implants obtained by additive manufacturing on osteoblastic adhesion and proliferation: a systematic review. Heliyon 2022;8:e12505.
[110] Ponader S, Vairaktaris E, Heinl P, Wilmowsky CV, Rottmair A, Körner C, et al. Effects of topographical surface modifications of electron beam melted Ti-6Al-4V titanium on human fetal osteoblasts. J Biomed Mater Res A 2008;84A:1111–9.
[111] Shaoki A, Xu J-Y, Sun H, Chen X-S, Ouyang J, Zhuang X-M, et al. Osseointegration of three-dimensional designed titanium implants manufactured by selective laser melting. Biofabrication 2016;8:045014.
[112] Tsukanaka M, Fujibayashi S, Takemoto M, Matsushita T, Kokubo T, Nakamura T, et al. Bioactive treatment promotes osteoblast differentiation on titanium materials fabricated by selective laser melting technology. Dent Mater J 2016;35:118–25.
[113] Ertorer O, Topping TD, Li Y, Moss W, Lavernia EJ. Nanostructured Ti consolidated via spark plasma sintering. Metall Mater Trans A Phys Metall Mater Sci 2011;42:964–73.
[114] Chaudhari R, Bauri R. Microstructure and mechanical properties of titanium processed by spark plasma sintering (SPS). Metall Microstruct Anal 2014;3:30–5.
[115] Beltrán AM, Civantos A, Dominguez-Trujillo C, Moriche R, Rodríguez-Ortiz JA, García-Moreno F, et al. Porous titanium surfaces to control bacteria growth: mechanical properties and sulfonated polyetheretherketone coatings as antibiofouling approaches. Metals 2019;9:995.
[116] Di Luca A, Longoni A, Criscenti G, Mota C, van Blitterswijk C, Moroni L. Toward mimicking the bone structure: design of novel hierarchical scaffolds with a tailored radial porosity gradient. Biofabrication 2016;8:045007.
[117] Morgan EF, Unnikrisnan GU, Hussein AI. Bone mechanical properties in healthy and diseased states. Annu Rev Biomed Eng 2018;20:119–43.